Review of Scientific Instruments

RESEARCH ARTICLE | FEBRUARY 28 2025

A spatial- and angle-resolved photoemission spectroscopy beamline based on capillary optics at ASTRID2

Alfred J. H. Jones ; Paulina Majchrzak ; Klara Volckaert ; Deepnarayan Biswas ; John Vad Andersen ; Søren V. Hoffmann ; Nykola C. Jones ; Zhihao Jiang ; Yong P. Chen ; Mads Lykke Jensen ; Rasmus Ørnekoll Stenshøj ; Marco Bianchi ; Philip Hofmann ; Søren Ulstrup ; Jill A. Miwa

Rev. Sci. Instrum. 96, 025109 (2025)
https://doi.org/10.1063/5.0240744

AIP Publishing

Review of Scientific Instruments ARTICLE pubs.aip.org/aip/rsi

A spatial- and angle-resolved photoemission spectroscopy beamline based on capillary optics at ASTRID2

Cite as: Rev. Sci. Instrum. 96, 025109 (2025); doi: 10.1063/5.0240744
Submitted: 26 September 2024 • Accepted: 30 January 2025 •
Published Online: 28 February 2025

Alfred J. H. Jones,[1] Paulina Majchrzak,[1] Klara Volckaert,[1] Deepnarayan Biswas,[1] John Vad Andersen,[1] Søren V. Hoffmann,[1] Nykola C. Jones,[1] Zhihao Jiang,[1] Yong P. Chen,[1,2] Mads Lykke Jensen,[1] Rasmus Ørnekoll Stenshøj,[1] Marco Bianchi,[4] Philip Hofmann,[1] Søren Ulstrup,[1] and Jill A. Miwa[1,4,a)]

AFFILIATIONS

[1] Department of Physics and Astronomy, Aarhus University, 8000 Aarhus C, Denmark
[2] Department of Physics and Astronomy and School of Electrical and Computer Engineering and Purdue Quantum Science and Engineering Institute, Purdue University, West Lafayette, Indiana 47907, USA
[3] Elettra-Sincrotrone Trieste SCpA, 34149 Basovizza, Italy
[4] Interdisciplinary Nanoscience Centre (iNano), Aarhus University, 8000 Aarhus C, Denmark

[a)] **Author to whom correspondence should be addressed:** miwa@phys.au.dk

ABSTRACT

Angle-resolved photoemission spectroscopy (ARPES) with spatial resolution is emerging as a powerful investigative tool for the study of operational mesoscale devices and quantum materials. Here, we introduce AU-SGM4, an extreme ultraviolet beamline based at the ASTRID2 synchrotron, which is designed around an achromatic elliptical capillary optic that focuses the synchrotron light down to a lateral beam spot size of 4 μm. The beamline offers a low photon energy range of 12–150 eV, ideal for probing detailed energy- and momentum-resolved electronic structures of materials. We utilize a custom-made piezoelectric motor system with 11 degrees of freedom for precisely moving the sample and capillary optic. We demonstrate exceptional stability in beam positioning on samples across the entire available photon energy range. To showcase the capabilities of the AU-SGM4 beamline, we present simultaneous ARPES measurements and *in situ* gating of a graphene device and probe the nominally inaccessible microscopic-sized domains of $MnBi_6Te_{10}$ to obtain the energy- and momentum-dependent dispersion for each domain.

I. INTRODUCTION

Angle resolved photoemission spectroscopy (ARPES) probes the energy- and momentum-resolved electronic excitation spectra of the occupied states in crystalline materials, which has contributed to the theoretical understanding of quantum materials such as unconventional superconductors, topological insulators, two-dimensional (2D) materials such as graphene and, more recently, kagome systems.[1–4] The technique is based on the photoelectric effect, wherein a photon impinges on the surface of a crystal, imparting energy to an electron in the material and promoting it from the valence band to a higher-energy state above the vacuum level.[5] These photoemitted electrons carry information about the electronic structure (binding energy and parallel momentum component) of the material due to conservation of energy and momentum.

A tunable photon energy probe, such as that provided by synchrotron radiation sources, can be desirable for many ARPES measurements, as control of the photon energy gives access to the perpendicular crystal momentum. The ability to control the probe energy also allows for the maximization of the cross section and matrix elements to best view a particular feature of the electronic band structure. Lower photon energies provide high energy

resolution for extracting detailed energy- and momentum-resolved information. In addition, the short inelastic mean free path of the photoemitted electrons at these energies confers a high degree of surface sensitivity to the ARPES measurements,[6,7] which can be useful when specifically studying surface-related phenomena or materials consisting of only a few atomic layers.

The ARPES photoemission intensity is proportional to the spectral function $A(E,k) = \frac{\pi^{-1}\Sigma''(E)}{(E-E_0(k)-\Sigma'(E))^2+\Sigma''(E)^2}$, where $E_0(k)$ is the bare band dispersion, and Σ' and Σ'' are the real and imaginary components of the electronic self-energy, respectively. Therefore, a detailed analysis of the measured energy-momentum dispersions may reveal additional parameters such as electron–phonon coupling strength and, in general, the presence of many-body effects can be inferred from linewidth changes and band renormalization.[1,8]

In recent years, there has been a growing emphasis on the modification of material systems out of equilibrium by various means, such as ultrafast laser pulses,[9–16] applied electric fields,[17–22] or strain.[23–25] Changes in the electronic structure can be measured by ARPES while applying these perturbations, which is necessary for understanding and further tailoring these induced, novel properties. Control of stacking order and twist angle in (2D) heterostructures provides a wide array of new moiré physics and can act as quantum simulators with designed properties.[26,27]

To access such out-of-equilibrium systems and tailored quantum materials often requires a smaller extreme ultraviolet beam than is available with traditional ARPES methods.[28,29] Functional mesoscale devices, for example, a back-gated graphene device, have typical uniform regions of less than 10 μm^2, and the inhomogeneous electric fields generated during operation of such devices will cause the photoelectron kinetic energy distribution to be broadened. These factors become increasingly impactful as the beam spot increases to the 20–100 μm typical of high-resolution ARPES setups.[21,30] A small beam spot significantly mitigates the issue of spectral broadening[17,18] and allows for focused attention to specific aspects of the device, including following electrostatic effects across a device with lateral current flow[31,32] [see Fig. 1(a)].

Similarly, 2D stacked heterostructure material systems are often small in size and show spatially dependent phenomena, particularly at interface regions and edges, due to exfoliation and stacking procedures used to produce them. Rotational inhomogeneity in twisted 2D heterostructures or bottom-up grown monolayers by methods such as chemical vapor deposition can severely broaden measured spectra;[21,33] therefore, to measure moiré heterostructure systems, such as magic angle twisted bilayer graphene, a small beam spot size is needed to isolate photoemission spectra from a uniformly twisted region.[34–36] Artificially engineered superlattices also require a small beam spot to determine the influence of the superlattice and applied electric field on the electronic structure.[37] Bulk crystals cleaved under ultra-high vacuum conditions, as illustrated in Fig. 1(b), may also feature domains of different surface terminations[38–41] or phases[42,43] on micrometer length scales.

In order to access this range of systems, ARPES with spatial resolution, referred to as microARPES or nanoARPES depending upon the achieved beam spot size, has been developed. This technique is available at a small number of synchrotron facilities around the world.[44–49] The most common method used for achieving a small beam spot size is the Fresnel zone plate. This diffractive optic

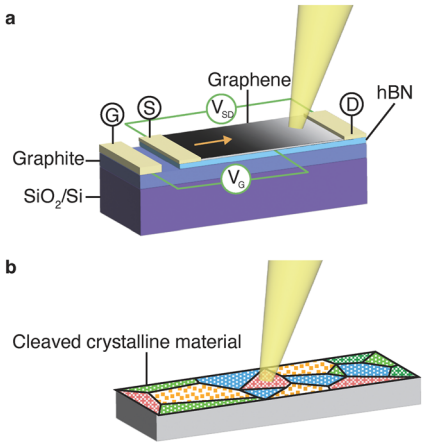

FIG. 1. (a) Illustration of a back-gated graphene device. The structure of the device is graphene on hBN, back-gated by graphite, sitting on a Si/SiO_2 substrate. The gold source (S), drain (D), and gate (G) electrodes are labeled. The beam is represented by the yellow cone. If a lateral current (orange arrow) is passed through the graphene via the S and D electrodes, a voltage (V_{SD}) drop (gradient) across the sample is observed.[31] Doping of the sample is achieved by applying a voltage V_G between the gate electrode and the sample. (b) Illustration of a cleaved crystalline material that exhibits microscopic domains with different surface terminations that may be accessed by a small beam spot size.

is made of lithographically patterned concentric rings, which have been shown to provide a mere 120 nm lateral size.[46,48,50] Despite the ability to achieve an exceptionally small beam spot size, these optics are highly inefficient, transmitting less than 10% of the coherent fraction of the beam, which at third generation synchrotrons is itself only a fraction of the full beam intensity. The focal distance and efficiency also change with the photon energy, so Fresnel zone plates cannot be used to probe the k_z dispersion of bulk crystals, where continuous variation of the photon energy is a requirement. Finally, an order sorting aperture (OSA) needs to be placed between the optic and the sample to block undiffracted light, which physically limits the range of motion and angular rotation of the sample relative to the electron analyzer. Other methods that have successfully produced sub-micrometer beam spot sizes include Schwarzschild optics:[44] pairs of normal incidence dielectric coated mirrors, which can provide about 10% transmission and less than 1 μm beam spot size. However, each pair of optics is only reflective at a single photon energy, limiting their versatility. Another alternative, Kirkpatrick–Baez (KB) mirrors, are pairs of cylindrical grazing incidence mirrors that provide an achromatic and high transmission focus as small as 10 μm for ARPES setups.[51]

A new method to obtain a small beam spot size with high transmission is based around an x-ray capillary optic.[47] These are hollow glass tubes with the internal surface coated in platinum acting as a mirror. The optics are placed very close (on the order of millimeters) to the sample being measured, where they demagnify a diverging source onto the focal plane. These optics have significantly higher transmission than either Fresnel zone plates or Schwarzschild optics. Moreover, they are achromatic; that is, they do not vary in

focal depth with photon energy. The high transmission and achromaticity mean that in a given measurement time a greater range of sample parameters (e.g., photon energies and, therefore, k_z dispersion, k_x and k_y ranges, gate voltage, and sample positions) may be explored in greater detail, making these highly versatile optics. To date, the smallest reported beam spot size with a capillary measured in a photoemission type geometry is 1.8 μm^2.[52]

This article introduces AU-SGM4, a new beamline at the ASTRID2 synchrotron designed for spatial- and angle-resolved photoemission spectroscopy, based on a capillary optic. Named for being the fourth spherical grating monochromator (SGM) beamline at ASTRID2, AU-SGM4 represents an advancement in the facility's capabilities.[30,36,41,53] Section I provides context and motivation for AU-SGM4. Section II details (A) the beamline design and its characterization, (B) the end-station, (C) the capillary optic, its behavior, and sample manipulation with piezoelectric motors, and (D) the determination of the beam spot size produced by the capillary optic. In Sec. III, two science cases are presented to demonstrate the capabilities of AU-SGM4: (A) a three-terminal monolayer graphene device and (B) a cleaved crystal of the layered topological insulator $MnBi_6Te_{10}$. Section IV provides a brief summary.

II. IMPLEMENTATION OF SPATIALLY RESOLVED ARPES AT ASTRID2

A. SGM4 beamline design and characterization

The AU-SGM4 beamline is built to utilize a capillary optic to achieve a few-micron beam spot size for spatially resolved ARPES measurements. Attached to the ASTRID2 synchrotron, a 580 MeV third generation facility,[54] it makes use of a variable photon energy range of 12–150 eV, delivered via a U55 type undulator.[55] In Fig. 2, a schematic of the AU-SGM4 beamline is presented, with the key components labeled. Two initial focusing mirrors, the horizontal focusing mirror (HFM) and the vertical focusing mirror (VFM), direct the beam onto the entrance slit (ENS). A SGM with a fixed entrance slit and a movable exit slit (EXS) is used for the selection of the photon energy. After the EXS of the monochromator, there is an in-line gas cell for the calibration of the photon energy and resolution, before a pair of horizontal and vertical post-focusing mirrors (PFM-H and PFM-V). The final focusing of the beam with the capillary optic inside the end-station will be discussed in Sec. II D.

The AU-SGM4 monochromator, upcycled from the I4 beamline at MAXlab,[56] is based on three spherical gratings for low (LEG), medium (MEG), and high (HEG) energy ranges with 300, 700, and 1500 lines/mm, respectively, with each grating using the same fixed included angle of 162°. Calculations for the main contributions to monochromator resolution, i.e., slit width, spherical aberration (coma), slope errors, and diffraction effects, are shown for each grating in Fig. 3(a) for ENS and EXS set to 20 μm. The energy ranges displayed correspond to the accessible energies for each grating (color-coded: LEG = green, MEG = blue, and HEG = yellow) based on geometric constraints of the monochromator.

To determine the beamline resolution and to make the energy calibration to the monochromator angle, an ionizing gas cell, sketched in Fig. 3(b), was placed after the EXS. Measurements of the neon $2P_{1/2}$ autoionization resonances, with energies corresponding to the minimum resolution of the LEG at about 21 eV, and the helium two-electron resonances on the MEG around 65 eV, are shown in Figs. 3(c) and 3(d). The neon autoionization spectra form sets of double peaks due to there being either ns' or nd' Rydberg electrons.[58] From Lorentzian fits applied to the first three doublet peaks of neon in the LEG, a linewidth of 2.5 ±0.4 meV was determined [see Fig. 3(c)], compared to the predicted width of 2.5 meV from Fig. 3(a). Similarly, the falling edge of the Fano profiles from the helium double ionization peaks, shown in Fig. 3(d), was fit using a step function convoluted with a Gaussian. These fit profiles, overlaid in red, converge to a value of 5.1 ± 0.7 meV in the MEG, while the calculation in Fig. 3(a) gives a value of 7.9 meV. The discrepancy here may be due to the entrance and exit slit terms being dominant, leading to an overestimate in the calculated resolution.

Following the monochromator and gas cell, a pair of post-focusing mirrors guide the beam through a small rectangular intermediate focus (IMF) chamber into the main chamber of the end-station, as shown in Fig. 4(a). These two cylindrical mirrors create an IMF, denoted by the blue-colored "×," 750 mm before the center of the end-station. The beam diverges from the IMF to fully illuminate the back of the capillary optic inside the main chamber, which demagnifies the IMF by a factor of 40 to produce the final

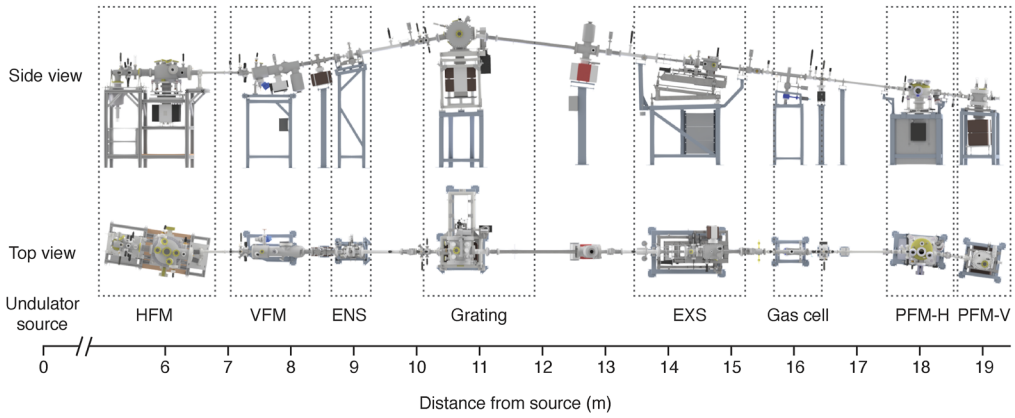

FIG. 2. Side and top view of the AU-SGM4 beamline with key optical components noted. All distances are given in meters from the undulator source.

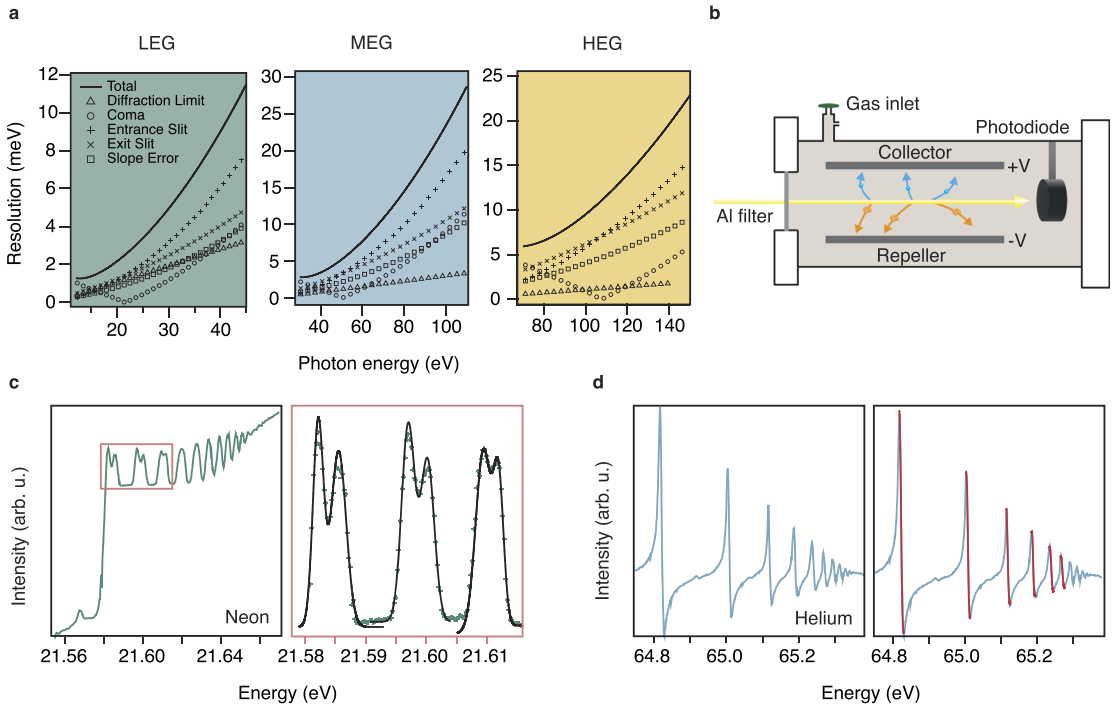

FIG. 3. Characterization of the AU-SGM4 beamline. (a) Calculated contributions to the energy resolution, using the methods of Ref. 57, for the LEG, MEG, and HEG. (b) Illustration of the in-line ionizing gas cell with electrons (blue) and ions (orange) produced by autoionization. (c) Measured $^2P_{1/2}$ autoionization spectra of neon (green) for the LEG and a zoomed-in view of the first three peaks, fitted with Lorentzian curves in black. (d) Measured autoionization peaks of doubly excited helium (blue) acquired in the MEG (left), and these peaks overlaid with a fit to the falling edge in red (right).

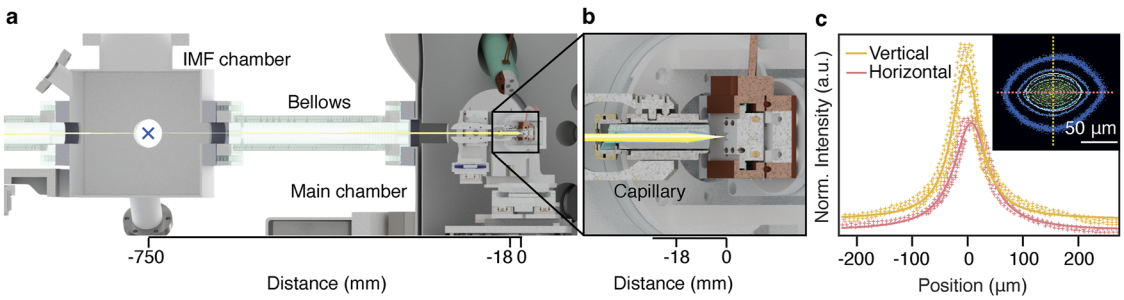

FIG. 4. Characterization of the intermediate focus (IMF). (a) Illustration of the focusing geometry from the post optics PFM-V and PFM-H through the IMF (marked with a cross) and into the main chamber of the end-station. Distances (in millimeters) from the capillary center and IMF are given with respect to the center of the main chamber. (b) The cross section perspective offers a view of how the beam is focused through the capillary and onto the sample. (c) Horizontal (pink) and vertical (yellow) profiles of the IMF ("+" markers) fit to Lorentzian peaks (solid lines) measured on a fluorescent YAG crystal. The inset shows an image of the IMF, with a 50 μm scale bar.

spot size on the sample [see Fig. 4(b)]. The nominal IMF size was determined in order to diagnose any broadening of the beam compared to specifications, which would impact the final focus of the beamline. This was performed by placing a fluorescent yttrium aluminum garnet (YAG) crystal (MTI Corporation) at an angle of 45° to the beam inside the IMF chamber and imaging the fluorescing spot with a camera. The crystal was then translated along the beam direction until the minimum spot size was found. An image of the beam at the focus is presented in Fig. 4(c), with the size of the beam spot determined to be 78 × 59 μm^2 from Lorentzian fits to the horizontal (pink) and vertical (yellow) profiles, respectively. This value is likely an overestimate due to the roughness of the YAG crystal and the broadening of the beam through the width of the crystal. From these parameters, a final capillary beam spot size at full width at half maximum (FWHM) at normal incidence of 2.0 × 1.5 μm^2 is predicted.

B. AU-SGM4 end-station design

The AU-SGM4 end-station, shown in Fig. 5(a), requires high precision positioning for both the sample and the capillary optic. In addition, the beam spot position on the sample needs to be stable both against vibrations and long-term drift with time and beamline parameters such as photon energy to ensure that long, multi-dimensional datasets can be acquired from the same spot on the sample.[53] Access to a wide range of emission angles of the photoelectrons is also necessary for ARPES measurement, again while maintaining the same position of the beam spot on the sample.

The AU-SGM4 end-station is modular with three sections to facilitate repairs and future upgrades to the system [see Fig. 5(b)]. These sections are, from top to bottom: pumping chamber, main chamber, and electrical chamber. The upper pumping chamber, outfitted with an 800 l/s Edwards turbomolecular pump, two 300 l/s Gamma Vacuum ion pumps, and two titanium sublimation pumps, allows the chamber to reach a base pressure better than 2×10^{-10} mbar. The middle main chamber hosts a Phoibos 150 SAL hemispherical analyzer (SPECS GmbH), with electron deflector lenses capable of acquiring up to a maximum angular range of $\pm 15^{\circ}$ perpendicular to the analyzer entrance slit in the wide angle mode, with smaller angular ranges provided by higher resolution angular lens modes. The main chamber is equipped with vacuum feedthroughs for cryogenic cooling of the sample, a fast entry load lock (FELL), and a microchannel plate (MCP) for characterizing the focused beam. The FELL, seen in Fig. 5(a) and labeled component 4, has a garage that houses two samples and supports indirect heating of samples up to 300 °C as measured by a K-type thermocouple mounted on the load lock garage. In addition, samples can be mechanically cleaved using an in-vacuum screwdriver or tape. All of the electrical cabling from the sample and capillary stages in the main chamber is fed through a pedestal down to and through the electrical chamber. This lower electrical chamber is mounted on a vibrational damping Zanite base (BaseTek, LLC.) and connects to mechanical struts for coarse adjustment of the chamber positions.

Inside the main chamber, shown in cross section in Fig. 5(c), the sample manipulator and capillary optic manipulator are mounted on the pedestal that is decoupled from the outer main chamber via mounting on bellows directly onto the Zanite base plate. This both dampens the effect of vibrations on the system and allows for movement of the analyzer position independently from the beam and sample. To aid this, two axes of rotation are available to the analyzer via vacuum compatible, differentially pumped rotational feedthroughs (Thermionics Laboratory Inc). By rotating the main chamber, the polar angle of the analyzer can be rotated up to 45° around the sample, and the analyzer azimuthal angle can be rotated a full 90° to set the entrance slit between horizontal or vertical positions, relative to the horizontal beam polarization. This provides access to a wide range of *k*-space without disturbing the alignment of the beam on the sample. In combination with the scanning deflector lenses on the analyzer itself, this enables constant energy surfaces

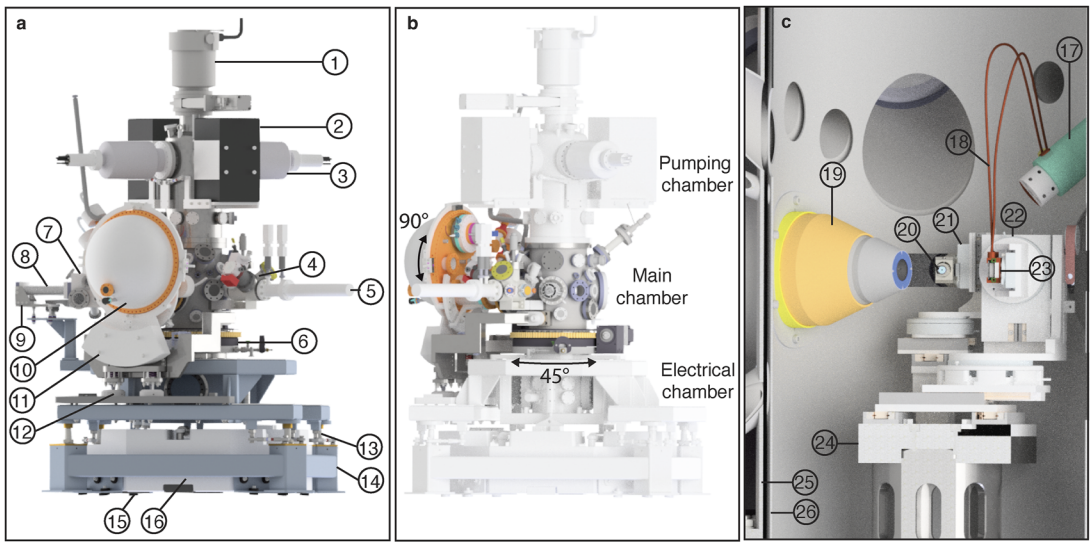

FIG. 5. Schematic of the AU-SGM4 end-station. (a) Overview of the outer chambers with salient components labeled. (1) 800 l/s Edwards turbomolecular pump. (2) 300 l/s Gamma vacuum ion pump. (3) Titanium sublimation pump. (4) Fast entry load lock with a two slot garage. (5) Telescopic load lock transfer arm. (6) Differentially pumped rotational feedthrough. (7) Intermediate focus (IMF) chamber. (8) Rectangular bellows (Mewasa AG). (9) Movable support for the IMF chamber. (10) SPECS Phoibos 150 SAL hemispherical analyzer. (11) Analyzer counterweight. (12) Air pads (MAGER S.r.l. Air Bearings). (13) Struts to mechanically adjust the frame position. (14) End-station support frame. (15) Anti-vibration pads (Sorbothane, Inc.). (16) Zanite block. (b) View of the end-station demarcating the three different modular sections. Rotational directions of the analyzer and the main chamber are indicated with arrows. (c) Interior of the main chamber with key components labeled. (17) Cryostat cold finger. (18) Fine gold-coated copper braids for cooling (Scienta Omicron). (19) Analyzer nose cone. (20) Capillary focusing optic. (21) 5-axis manipulation stage for the capillary optic. (22) 6-axis manipulation stage for the sample. (23) Sample socket. (24) Pedestal for capillary optic and sample manipulation stages. (25) Outer stainless steel wall of the main chamber (Thermionics Laboratory, Inc.). (26) Mu-metal shield (Amuneal Manufacturing Corp.).

to be efficiently surveyed without any movement of the beam or sample.

C. Capillary optic and sample manipulation with piezoelectric motors

The mounting of the capillary optic and sample manipulation stages is shown in Fig. 6(a), and the key components are labeled. The capillary optic is positioned by a five-axis manipulator (component 2), and the sample position is controlled by a six-axis manipulator (component 4). All motors are optically encoded stick-slip piezoelectrics (SmarAct GmbH), which can achieve better than 100 nm repeatable positioning over their entire travel range (i.e., several tens of millimeters), which are noted in Fig. 6(a). Similarly, rotational motors can achieve a wide angular range with better than 0.3 μrad positioning. The wide travel range allows access to the measurement position for a wide variety of sample sizes, the FELL, and a port for future sample preparation chambers. This highly precise, repeatable positioning is necessary for alignment of the capillary optic to the sample to fully utilize the small beam spot size. The tight geometry of the system has the end of the capillary only 7 mm from the sample surface at focus and the analyzer nose 35 mm from the sample. Overlap of the analyzer and beam foci is critical for optimal measurement and is controlled either by movement of the sample and capillary optic stage motors or via external struts on the outer chamber [see component 13 in Fig. 5(a)].

The sample socket, made from solid oxygen-free copper, is insulated from the sample manipulator by polyether ether ketone (PEEK) washers [see component 3 in Fig. 6(a)]. A schematic of the sample socket is shown in Fig. 6(b). This design ensures both electrical and thermal isolation. The sample holder features a minimalist design, consisting of a tantalum plate measuring 24.0 × 16.0 × 1.0 mm^3, bolted to an aluminum oxide support fitted with K-type thermocouple feet [Fig. 6(c)]. These feet serve a dual purpose: securing the sample holder within the sample socket and providing temperature readings of the sample during annealing in the FELL. The simplicity of the design allows for samples to be secured to the tantalum plate either through the use of silver epoxy or by spot welding with tantalum clips.

A custom-designed sample holder for use in in-operando measurements is presented in a diagram in Fig. 6(d). Mesoscale devices can be mounted on an eight-pin CSB00815 chip carrier (Spectrum

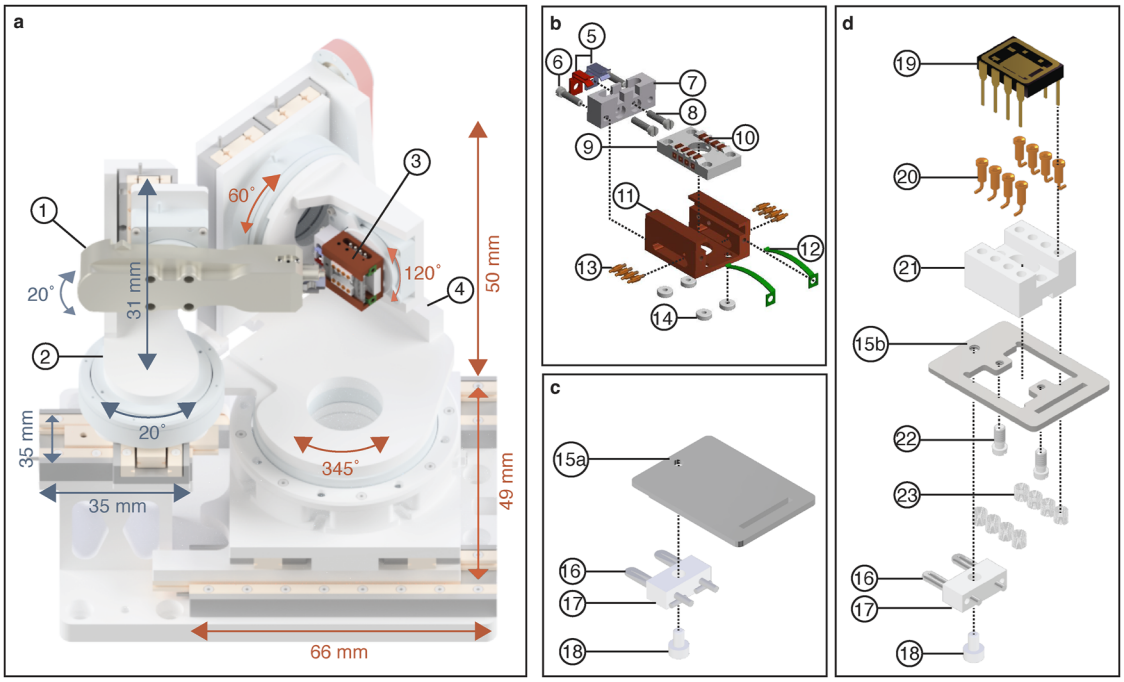

FIG. 6. Capillary optic and sample manipulation with piezoelectric motors. (a) Illustration of the five-axis capillary manipulator and the six-axis sample manipulator with salient components noted. Double-headed arrows indicate the available magnitude and directions of movement. (1) Titanium support for the capillary optic. (2) 5-axis capillary manipulator. (3) Sample socket. (4) 6-axis sample manipulator. (b) Diagram of the sample socket with all components labeled. (5) K-type thermocouple sockets made from alumel (blue) and chromel (red). (6) M2 titanium threaded bolt. (7) Aluminum oxide support. (8) M2 titanium threaded bolt. (9) PEEK support. (10) Oxygen-free copper electrical contacts for a custom-designed sample holder for in-operando measurements. (11) Solid oxygen-free copper sample support. (12) Beryllium copper springs to secure sample plates in the sample support. (13) Custom-made titanium connectors. (14) PEEK washers. (c) Diagram of the sample plate for cleavable samples. (15a) Tantalum sample plate. (16) K-type thermocouple legs. (17) Aluminum oxide support. (18) M2 molybdenum threaded bolt. (d) Diagram of the in-operando measurement sample holder. (19) Eight pin CSB00815 chip carrier. (20) Gold-coated copper dual in-line package (DIP) sockets. (21) Macor support for DIP sockets. (22) M1.6 molybdenum threaded bolts. (23) Tantalum springs. [Note: The sample plates in (c) and (d) are not to scale with respect to the sample socket in panel (b).]

Semiconductor Materials) with device electrodes wire-bonded to metallic pads on the chip carrier. The legs of the chip carrier are nested in gold-coated socket pins (component 20), secured in a Macor support with a large central hole for better annealing of the device's active material. The Macor support, bolted to a modified tantalum plate (component 15b), provides electrical isolation for the chip carrier from the tantalum plate. Each socket pin's end is connected to a spring (component 23) protruding from the Macor support, enabling a sliding electrical connection with the sample socket. This setup allows for up to eight different electrical connections to be made in a vacuum to a given device. External voltages are applied using Keithley 2450 source meters.

D. Determining the beam spot size produced by the capillary optic

The focusing element used in the AU-SGM4 end-station is a platinum-coated, elliptical capillary optic (Sigray, Inc.).[47] The entrance and exit apertures of the capillary are 3.36 and 1.64 mm, respectively, with a length of 25.8 mm and a working distance of 7.8 mm. This design provides a high numerical aperture for a predicted demagnification of the intermediate focus of ×40 with a transmission of ~30% between 20 and 70 eV and 25% above 100 eV. The capillary was selected over other previously mentioned focusing optics, e.g., Fresnel zone plates or Schwarzschild optics, due to its achromaticity and high transmission.

Fine alignment of the capillary is performed by measuring the far field beam on the MCP 150 mm downstream from the center of the main chamber. This produces an inverted image of the back of the capillary as shown in Fig. 7(a). The image being inverted means that the outer regions illuminated on the MCP correspond to the exit of the optic close to the sample, while the inner circle corresponds to the entrance of the capillary. The bright spot in the very center is a diffraction effect, a Fresnel or Arago spot. By translating a gold-coated knife edge (not shown) through the beam, the beam diameter can be determined from the occlusion of the image on the MCP. (A video and several snapshots of a typical measurement are included in the supplementary material.) The differential of this knife edge intensity profile is the beam profile, assuming a perfectly sharp knife edge. Horizontal (pink) and vertical (yellow) beam profiles of the beam at focus are presented in Fig. 7(b), where each dataset has been fitted to a Lorentzian curve, demonstrating an optimal FWHM of $4.3 \times 3.9\ \mu m^2$. Away from focus, the beam diverges into individual components, as can be seen in the upper and lower sections of the left plot in Fig. 7(c), where the differential intensity profile is given at different focal distances over a 200 μm range. Only at the beam focus do all these components converge. The angular alignment of the capillary is also critical for achieving the best possible focus. The plot to the right of Fig. 7(c) shows the same differential intensity profile across a 50 m° range of capillary angles, where the beam doubles in size with a misalignment of 10 m°. This emphasizes the importance of precise control of the capillary alignment when measuring. Additional measurements of the differential beam intensity with capillary angles are presented in Fig. S3 of the supplementary material. To improve the focus behavior, an optional larger beam stop may be introduced to the back of the capillary, reducing the transmission of the optic but removing satellite peaks.

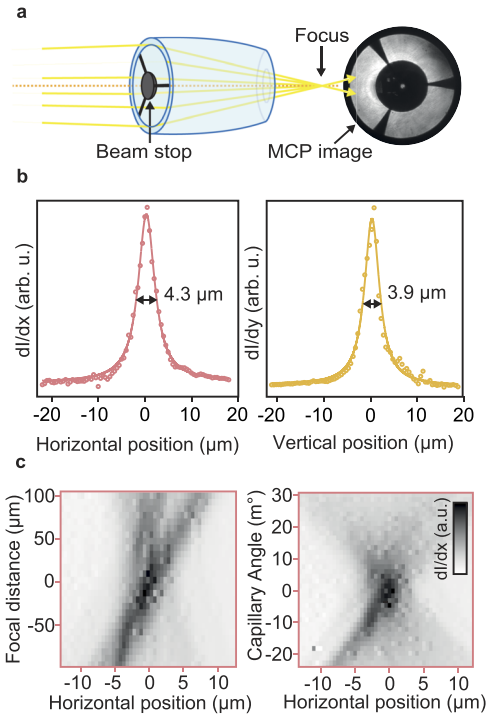

FIG. 7. Measured behavior of the capillary optic. (a) Schematic diagram of the focusing geometry for the elliptical capillary optic. An image of the fully illuminated capillary on the MCP is shown to the right. (b) Horizontal (pink markers) and vertical (yellow markers) profiles of the beam at focus, fitted to a Lorentzian curve (solid lines). Both profiles were measured with a beam stop in place. (c) Horizontal differential profile of the beam as a function of distance from the focus (left) and as a function of the vertical tilt of the capillary (right).

The spatial resolution determined in transmission geometry using the knife edge was confirmed by test measurements in the typical photoemission measurement geometry, with the sample positioned at an angle of 45° to the beam. A patterned gold sample, specifically fabricated for testing the spatial resolution, is shown in the optical microscope image of Fig. 8(a). It consists of a series of circles of decreasing sizes, ranging from the largest diameter of 200.0 μm to the smallest diameter of 2.5 μm. A zoom-in of the smallest circles is shown within the orange frame. For the photoemission measurement, the summed photoemission intensity at normal emission was mapped while the sample was raster scanned with the piezoelectric motors relative to the beam. The measured photoemission map, presented to the right of the optical microscope images, reproduces the features. A zoom-in on the smallest circles, ranging from 40.0 μm down to 2.5 μm, again reproduces the optical measurement and indicates agreement with the beam spot size as determined from the knife edge measurement. The additional rectangular areas of the patterned gold sample—seen only in the optical microscope image—were then used to determine the horizontal (pink) and vertical (yellow) diameters of the beam, using the same differential profile as with the knife edge measurements in Fig. 7. A FWHM of $8.3 \times 4.2\ \mu m^2$ was measured from Lorentzian fits to the photoemission data. The observed horizontal broadening, relative to the

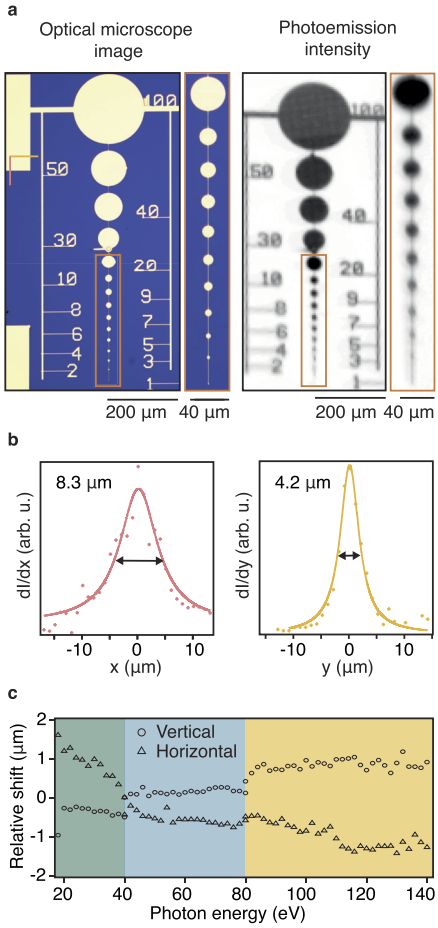

FIG. 8. Photoemission characterization of the beam spot size. (a) Optical microscope image of the patterned gold sample (left) and photoemission sum intensity map of the sample area (right). (b) Differential of a horizontal line profile along the gold rectangle at the top left of the optical microscope image (pink line) fit to a Lorentzian curve (solid line). Differential of a vertical line profile (yellow line) fit similarly to the horizontal one but along the yellow line over the gold rectangle edge. (c) Movement of edge position horizontally (triangles) and vertically (circles) over the full energy range of the monochromator, relative to the position at 40 eV on the MEG. The different gratings are marked with different colors: LEG = green, MEG = blue, and HEG = yellow.

knife-edge measurement, is attributed to the 45° angle between the sample and the beam. On a perfectly flat surface, the beam would be expected to broaden by $\sqrt{2}$. However, because the horizontal edge was aligned at an angle to the beam translation direction, additional broadening was observed.

When measuring at varying photon energies, the relative position of the beam and sample should remain unchanged. To confirm stability with photon energy, spatial maps around the corner of the rectangle in the upper left optical microscope image in Fig. 8(a) were made across the full photon range of all three gratings of the monochromator. The position of the horizontal and vertical edge of the corner was determined with a step function convoluted with a Gaussian to describe the beam-broadened step edge. The change in this edge position as a function of photon energy is plotted in Fig. 8(c) with the different gratings colored separately. The full shift across the entire photon energy range is less than half the FWHM of the beam, demonstrating a stability more than sufficient to perform photon energy scans on samples at the limit of resolution. Similarly, the stability of the sample-beam position with rotation of the analyzer across its full 45° travel was measured to be <1 μm both horizontally and vertically, confirming no influence of this rotation on the sample position.

III. APPLICATIONS OF SPATIALLY RESOLVED ARPES AT AU-SGM4

A. Electronic structure of *in situ* gated graphene device

As a demonstration of the in-operando measurement capability at AU-SGM4, a three-terminal monolayer graphene device was used. Such devices have previously been characterized using ARPES with nanoscale spatial resolution to extract the doping dependent quasiparticle dispersion when the filling of the Dirac cone is tuned via electrostatic gating.[17–19,59] The device geometry used here, shown in the optical microscope image of Fig. 9(a), comprises a graphite back gate (dark blue) placed under a 25 nm-thick hexagonal boron nitride (hBN) insulator (light blue) and a single layer of graphene (outlined in white), which itself is connected to the gold contacts via additional pieces of few-layer graphene. The entire stack of materials is supported by a SiO_2/Si substrate. Such a construction allows for measurement of the transverse resistance of the graphene during electrostatic doping from the back gate. A sweep of the source–drain resistance vs gate voltage is shown in Fig. 9(b). The resistance (green markers) peaks at 78 kΩ at the gate voltage corresponding to the minimum Fermi surface radius (orange markers), as will be detailed later. This behavior confirms that the device is functional—with graphene doping controlled by the gate voltage—while the asymmetric line profile arises from measurement with the UV beam, as has been observed previously.[19]

The device was initially mapped by raster scanning the beam spot and collecting an (E, k)-resolved snapshot from each (x, y)-position. The sum intensity from such a raster scan is presented to the right of the optical microscope image for comparison. Note that only the three contacted gold pads (labeled gate, source, and drain) show intensity. The fourth unlabeled contact pad, in the lower left, is not electrically connected and, therefore, not visible in photoemission due to charging. Regions of graphite, hBN, and graphene were identified by their differing spectral features. From examination of the full 4D (E, k, x, y)-dependent map of the device, the region with the highest quality monolayer graphene spectrum, as determined by the linewidth of the dispersion, was selected for further measurements and marked with a star. All measurements were made at a photon energy of 47 eV.

With the optimum spot located, a voltage was then applied to the graphite back gate to electrostatically dope the graphene. Maximum and minimum voltages were determined from the onset of a leakage current through the hBN. The analyzer deflectors were used to acquire 3D (E, k_x, k_y)-dependent spectra around the Dirac cone for the range of applied gate voltages, i.e., -8.0 to +9.0 V. Cuts through the center of the Dirac cone for three cases: maximum p-type doping, no applied gate voltage, and maximum n-type doping

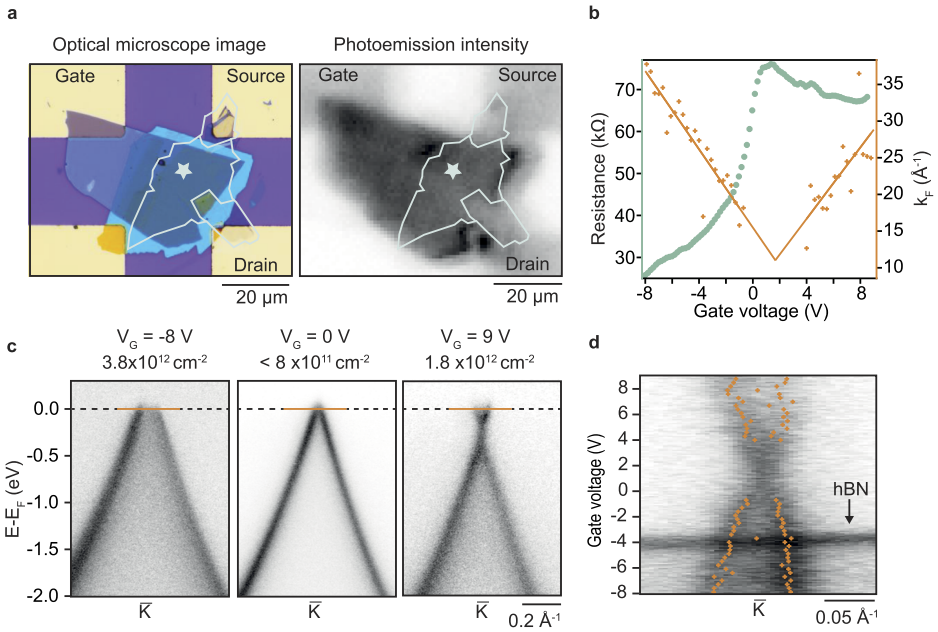

FIG. 9. Measuring a three-terminal monolayer graphene device. (a) Optical microscope image of the device shown to the left. The source, drain, and gate electrical contacts are labeled, and the graphene region is demarcated in white. The photoemission sum intensity map of the same area of the device is shown to the right. The star indicates the region with the highest observed graphene quality, used for the following measurements. (b) Resistance and Fermi surface radius as a function of applied gate voltage. The source–drain resistance under the application of a 50 mV source–drain voltage is represented by the green markers. The orange markers show the determined Fermi surface radius. (Note that this measurement was performed during the photoemission measurements.) The solid orange line is a linear fit to the acquired data. (c) From left to right, the photoemission spectra through the center of the Dirac cone when the graphene is maximally *p*-doped, not gated, and maximally *n*-doped. (d) MDCs as a function of gate voltage, extracted from the Fermi level on the Dirac cone, as shown by the orange lines in (c). The hBN band is highlighted by the black arrow, while maxima of Lorentzian fits to obtain the Fermi wavevector k_F are marked with orange crosses.

are presented in Fig. 9(c), from left to right. The amount of doping, calculated from the Fermi surface area using $n = k_F^2/\pi$, where k_F is the Fermi surface radius, is noted above each spectrum.[19] In these measurements, it was key to extract the full 3D spectrum of the Dirac cones, as the electric field from the back gate led to a shift in the emission angles measured in the analyzer. These shifts uniformly displace the emitted electrons in emission angle and do not appear to distort the measured spectrum. Following the alignment of the Dirac cones to account for the shifts, a momentum distribution curve (MDC) at the Fermi level (solid orange line) was taken for each applied gate voltage [see Fig. 9(d)]. This plot illustrates the change in Fermi surface area as the carrier concentration is varied. k_F values were extracted from the maximum of the MDCs and noted with orange crosses. The region near charge neutrality could not be adequately fit due to the closeness of the two branches, providing a lower limit of the directly calculable carrier concentration with this method. The almost horizontal band, labeled with a black arrow, is the hBN, which follows the potential of the gate. The measured k_F is plotted on top of the measured gate resistance in Fig. 9(b) and fit to a linear function (solid orange line), showing the expected ambipolar doping with a minimum around 1.65 V, corresponding to a slight *p*-doping of the sample at a gate voltage of 0 V.

These results demonstrate the capability to extract high quality photoemission spectra from an operational device, with the small beam spot size enabling measurement with minimal distortion from the applied electric field or native sample surface inhomogeneity. High-dimensional data acquisition also enables the tracking of key features, such as a continuous view of the doping with gate voltage and the movement of van Hove singularities in twisted bilayers.[20] The high quality of the spectra obtained from this reversible electrical doping enables measurement of doping-dependent changes to the electron–phonon coupling and other many body effects.[19]

B. Surface termination-dependent electronic structure of a quantum material

The capabilities of AU-SGM4 are showcased through measurements of the surface electronic structures of the layered magnetic topological insulator, $MnBi_6Te_{10}$. This material is made up of septuple layers (SLs) of magnetic $MnBi_2Te_4$[60] separated by two Bi_2Te_3 quintuple layers (QL),[41,61,62] as diagrammed in Fig. 10(a). The SL has realized Chern and axionic insulator states and the realization of the quantum anomalous Hall effect.[63,64] Intercalation of QL weakens the interlayer interactions and leads to a spin flop transition from the antiferromagnetic SL to a ferromagnetic state, demonstrating exciting interplay between topological and magnetic properties.[41,65] Upon cleaving in vacuum, such crystals often produce an irregular surface, as emphasized by the optical microscope image (left panel) of Fig. 10(b). This irregular surface displays a range of different

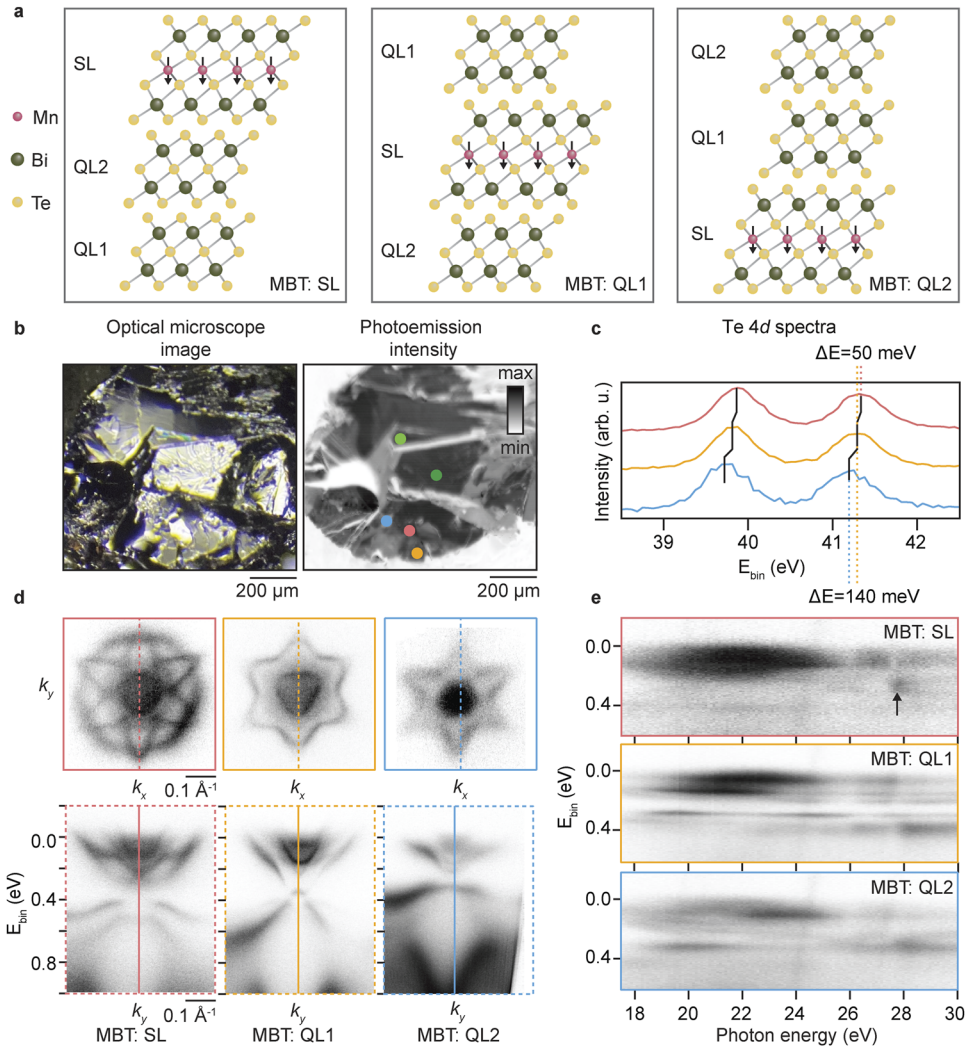

FIG. 10. Identifying the different surface terminations of a cleaved $MnBi_6Te_{10}$ crystal (MBT). (a) Diagram of the three possible surface terminations of MBT. (b) An optical microscope image of MBT following cleaving is shown to the left. The photoemission integrated intensity map is shown to the right, with parameters selected to maximize the contrast between regions of different surface termination. Colored markers indicate different measured regions displaying different chemical and electronic structures. The green dots indicate areas of non-intercalated Bi_2Te_3. (c) Spectra of the Te 4*d* core level collected at the positions marked by color-coded dots in the photoemission integrated intensity map in (b). A photon energy of 145 eV was used to acquire the core level data. (d) Top row: Fermi surface for each surface termination. Bottom row: (E, k) dispersion along the high-symmetry direction marked with a dashed line for the three surface terminations. A photon energy of 21 eV was used to collect the photoemission spectra in (d). (e) Photon energy dependence of an EDC through the Γ point of each termination, marked with a solid line in (d).

surface terminations, which are expected to produce unique electronic band dispersions.[61,65]

The large range of the piezo scanning stage permits locating the sample on the 16 × 25 mm^2 sample plate using a step size of 200 μm to identify an area of 1 mm^2 corresponding to the cleaved region, using the intensity close to the Fermi level (not shown). Afterward, the sample area was raster scanned with a smaller step size of 5 μm, approximately the size of the beam spot, to elucidate fine details of the cleaved surface. From each position on the sample, a single (E, k)-snapshot was obtained. To the right of the optical microscope image in Fig. 10(b), the photoemission intensity integrated over a region of interest around the center of the Brillouin zone is presented for comparison to the optical image. Correlation between the areas of uniform intensity in the photoemission intensity map and the optical microscope image is apparent. To understand the chemical composition, an analogous map was collected at a photon energy of 145 eV while monitoring the relevant Te 4*d* core levels. Representative lineshapes of the Te 4*d* peak are plotted in Fig. 10(c) for selected areas marked with color-coded dots in Fig. 10(b), displaying a range of peak positions. It is expected that different surface terminations would exhibit different peak positions due to surface selectivity.

From the combination of valence and core level spatial maps of the crystal, a number of different chemical compositions and surface terminations are revealed. High quality Fermi surfaces taken from selected sample regions are presented in the top row of Fig. 10(d). The Fermi contours closely resemble those previously reported in Refs. 66–68 for the SL and single- and double-QL surface terminations of $MnBi_6Te_{10}$, denoted as MBT:QL1 and MBT:QL2, respectively. To further highlight the electronic differences in the surface terminations, (E, k)-dispersions extracted from the presented constant Fermi contours along the crystal's high-symmetry direction, marked by the dashed lines, are included.

Varying the incident photon energy modulates the photoemission matrix element, often providing access to additional information about the material's symmetry[69,70] and the out-of-plane momentum component, k_z, in bulk materials. Energy distribution

curves (EDCs) taken at normal emission are presented in Fig. 10(e) for each of the three terminations. Dispersion is not observed in the three cases, either because of a lack of k_z dispersion or intrinsic k_z smearing. However, the photoemission intensity as a function of photon energy changes significantly as the matrix elements for different bands vary. Nevertheless, it is clear that the same states are tracked across the entire photon energy range, highlighting the stability of the system demonstrated in Fig. 8(c). For the SL termination, the appearance of a "new" feature, marked by the black arrow, is observed and attributed to an apparent closing of a gap near 28 eV photon energy. Such insights into the spatial and photon energy dependent band dispersions underscore the capabilities of an energy-tunable, spatially resolved ARPES system based on a capillary optic.

IV. CONCLUSION

In summary, we introduce AU-SGM4, a capillary-based spatially resolved ARPES system established at the ASTRID2 light source. The achromatic capillary optic focuses the synchrotron light down to a lateral beam spot size of $4.3 \times 3.9\ \mu m^2$ (FWHM) as determined via knife edge measurements at normal incidence. Its achromaticity and remarkable stability in beam positioning on samples make it ideal for probing detailed energy- and momentum-resolved electronic structures of materials on mesoscopic length scales. To showcase the capabilities of AU-SGM4, simultaneous ARPES measurements and *in situ* gating of a graphene device are demonstrated, along with the probing of the surface electronic structure of the different microscopic terminations of the quantum material $MnBi_6Te_{10}$. The AU-SGM4 instrument provides spatially resolved ARPES based on a capillary optic giving access to the electronic properties of new classes of quantum materials and devices.

SUPPLEMENTARY MATERIAL

The supplementary material accompanies this paper, which includes additional information and data related to the knife edge measurements.

ACKNOWLEDGMENTS

The authors are grateful for the support from the mechanical workshop at the Department of Physics and Astronomy at Aarhus University during the design and construction of the AU-SGM4 beamline, as well as discussions on technical aspects with A. Bostwick, C. Jozwiak, E. Rotenberg, P. Dudin, M. Watson, and C. Cacho. We acknowledge MAXIV (previously MAXlab) and, in particular, B. Thiagarajan, J. Adell, M. Leandersson, and J. Andersen for the MaxLab I4 beamline, as well as D. Field for components from the former SGM2 beamline, which in large part comprise the AU-SGM4 beamline. We gratefully acknowledge J. W. Wells at the University of Oslo in Norway for fruitful discussions.

We acknowledge the hBN for the graphene device that was provided by K. Watanabe and T. Taniguchi under the grants JSPS KAKENHI (Grant Nos. 21H05233 and 23H02052) and World Premier International Research Center Initiative (WPI), MEXT, Japan. We acknowledge X.-C. Pan from the Advanced Institute for Materials Research at Tohoku University in Japan for the $MnBi_6Te_{10}$ samples. The authors acknowledge funding from the Danish Council for Independent Research, Natural Sciences under the Sapere Aude program (Grant Nos. DFF-6108-00409 and DFF-9064-00057B), the Aarhus University Research Foundation, and VILLUM FONDEN through the Young Investigator Program (Grant No. 15375), Villum Investigator Program (Grant No. 25931), and the Center of Excellence for Dirac Materials (Grant No. 11744). Work at the Advanced Institute for Materials Research has benefited from the support of WPI-AIMR, JSPS KAKENHI Basic Science A (Grant Nos. 22H00278, 21K18590, 20H04623, 18H04473, 18H03858, and 18F18328), and the Tohoku University FRiD program.

AUTHOR DECLARATIONS

Conflict of Interest

The authors have no conflicts to disclose.

Author Contributions

Alfred J. H. Jones: Conceptualization (lead); Data curation (equal); Investigation (equal); Writing – original draft (lead); Writing – review & editing (lead). **Paulina Majchrzak**: Conceptualization (equal); Data curation (equal); Investigation (equal); Writing – original draft (supporting); Writing – review & editing (supporting). **Klara Volckaert**: Conceptualization (equal); Data curation (equal); Investigation (equal); Writing – review & editing (supporting). **Deepnarayan Biswas**: Conceptualization (equal); Data curation (equal); Investigation (equal); Writing – review & editing (supporting). **John Erik Vad Andersen**: Conceptualization (equal); Writing – review & editing (supporting). **Søren V. Hoffmann**: Conceptualization (supporting); Investigation (supporting); Writing – review & editing (supporting). **Nykola C. Jones**: Conceptualization (supporting); Investigation (supporting); Writing – review & editing (supporting). **Zhihao Jiang**: Data curation (supporting); Investigation (supporting); Writing – review & editing (supporting). **Yong P. Chen**: Resources (supporting); Writing – review & editing (supporting). **Mads Lykke Jensen**: Data curation (supporting); Investigation (supporting); Writing – review & editing (supporting). **Rasmus Ørnekoll Stenshøj**: Data curation (supporting); Investigation (supporting); Writing – review & editing (supporting). **Marco Bianchi**: Conceptualization (supporting); Writing – review & editing (supporting). **Philip Hofmann**: Conceptualization (supporting); Data curation (supporting); Funding acquisition (supporting); Investigation (supporting); Writing – review & editing (supporting). **Søren Ulstrup**: Conceptualization (lead); Data curation (equal); Funding acquisition (lead); Investigation (equal); Writing – review & editing (equal). **Jill A. Miwa**: Conceptualization (lead); Data curation (equal); Funding acquisition (lead); Investigation (equal); Writing – original draft (lead); Writing – review & editing (lead).

DATA AVAILABILITY

The data that support the plots within this paper and other findings of this study are available from the corresponding author upon reasonable request.

REFERENCES

[1] A. Damascelli, Z. Hussain, and Z.-X. Shen, "Angle-resolved photoemission studies of the cuprate superconductors," Rev. Mod. Phys. **75**, 473–541 (2003).

[2] J. A. Sobota, Y. He, and Z.-X. Shen, "Angle-resolved photoemission studies of quantum materials," Rev. Mod. Phys. **93**, 025006 (2021).

[3] A. Bostwick, T. Ohta, T. Seyller, K. Horn, and E. Rotenberg, "Quasiparticle dynamics in graphene," Nat. Phys. **3**, 36–40 (2007).

[4] L. Ye, M. Kang, J. Liu, F. von Cube, C. R. Wicker, T. Suzuki, C. Jozwiak, A. Bostwick, E. Rotenberg, D. C. Bell, L. Fu, R. Comin, and J. G. Checkelsky, "Massive Dirac fermions in a ferromagnetic kagome metal," Nature **555**, 638–642 (2018).

[5] S. Hüfner, *Photoelectron Spectroscopy: Principles and Applications*, 3rd ed. (Springer, Berlin, 2003).

[6] M. P. Seah and W. A. Dench, "Quantitative electron spectroscopy of surfaces: A standard data base for electron inelastic mean free paths in solids," Surf. Interface Anal. **1**, 2–11 (1979).

[7] J. A. Miwa, P. Hofmann, M. Y. Simmons, and J. W. Wells, "Direct measurement of the band structure of a buried two-dimensional electron gas," Phys. Rev. Lett. **110**, 136801 (2013).

[8] S. Hüfner, *Very High Resolution Photoelectron Spectroscopy*, 1st ed. (Springer, Berlin, 2007).

[9] M. Sentef, A. F. Kemper, B. Moritz, J. K. Freericks, Z.-X. Shen, and T. P. Devereaux, "Examining electron-boson coupling using time-resolved spectroscopy," Phys. Rev. X **3**, 041033 (2013).

[10] F. Boschini, M. Zonno, and A. Damascelli, "Time-resolved ARPES studies of quantum materials," Rev. Mod. Phys. **96**, 015003 (2024).

[11] R. Krause, S. Aeschlimann, M. Chávez-Cervantes, R. Perea-Causin, S. Brem, E. Malic, S. Forti, F. Fabbri, C. Coletti, and I. Gierz, "Microscopic understanding of ultrafast charge transfer in van der Waals heterostructures," Phys. Rev. Lett. **127**, 276401 (2021).

[12] H. Hübener, M. A. Sentef, U. De Giovannini, A. F. Kemper, and A. Rubio, "Creating stable Floquet–Weyl semimetals by laser-driving of 3D Dirac materials," Nat. Commun. **8**, 13940 (2017).

[13] A. Grubišić Čabo, J. A. Miwa, S. S. Grønborg, J. M. Riley, J. C. Johannsen, C. Cacho, O. Alexander, R. T. Chapman, E. Springate, M. Grioni, J. V. Lauritsen, P. D. C. King, P. Hofmann, and S. Ulstrup, "Observation of ultrafast free carrier dynamics in single layer MoS_2," Nano Lett. **15**, 5883–5887 (2015).

[14] S. Ulstrup, J. C. Johannsen, F. Cilento, J. A. Miwa, A. Crepaldi, M. Zacchigna, C. Cacho, R. Chapman, E. Springate, S. Mammadov, F. Fromm, C. Raidel, T. Seyller, F. Parmigiani, M. Grioni, P. D. C. King, and P. Hofmann, "Ultrafast dynamics of massive Dirac fermions in bilayer graphene," Phys. Rev. Lett. **112**, 257401 (2014).

[15] D. Biswas, A. J. H. Jones, P. Majchrzak, B. K. Choi, T.-H. Lee, K. Volckaert, J. Feng, I. Marković, F. Andreatta, C.-J. Kang, H. J. Kim, I. H. Lee, C. Jozwiak, E. Rotenberg, A. Bostwick, C. E. Sanders, Y. Zhang, G. Karras, R. T. Chapman, A. S. Wyatt, E. Springate, J. A. Miwa, P. Hofmann, P. D. C. King, Y. J. Chang, N. Lanatà, and S. Ulstrup, "Ultrafast triggering of insulator–metal transition in two-dimensional VSe_2," Nano Lett. **21**, 1968–1975 (2021).

[16] C. J. Sayers, G. Cerullo, Y. Zhang, C. E. Sanders, R. T. Chapman, A. S. Wyatt, G. Chatterjee, E. Springate, D. Wolverson, E. Da Como, and E. Carpene, "Exploring the charge density wave phase of 1*T*-$TaSe_2$: Mott or charge-transfer gap?," Phys. Rev. Lett. **130**, 156401 (2023).

[17] F. Joucken, J. Avila, Z. Ge, E. A. Quezada-Lopez, H. Yi, R. Le Goff, E. Baudin, J. L. Davenport, K. Watanabe, T. Taniguchi, M. C. Asensio, and J. J. Velasco, "Visualizing the effect of an electrostatic gate with angle-resolved photoemission spectroscopy," Nano Lett. **19**, 2682–2687 (2019).

[18] P. V. Nguyen, N. C. Teutsch, N. P. Wilson, J. Kahn, X. Xia, A. J. Graham, V. Kandyba, A. Giampietri, A. Barinov, G. C. Constantinescu, N. Yeung, N. D. M. Hine, X. Xu, D. H. Cobden, and N. R. Wilson, "Visualizing electrostatic gating effects in two-dimensional heterostructures," Nature **572**, 220–223 (2019).

[19] R. Muzzio, A. J. H. Jones, D. Curcio, D. Biswas, J. A. Miwa, P. Hofmann, K. Watanabe, T. Taniguchi, S. Singh, C. Jozwiak, E. Rotenberg, A. Bostwick, R. J. Koch, S. Ulstrup, and J. Katoch, "Momentum-resolved view of highly tunable many-body effects in a graphene/hBN field-effect device," Phys. Rev. B **101**, 201409 (2020).

[20] A. J. H. Jones, R. Muzzio, P. Majchrzak, S. Pakdel, D. Curcio, K. Volckaert, D. Biswas, J. Gobbo, S. Singh, J. T. Robinson, K. Watanabe, T. Taniguchi, T. K. Kim, C. Cacho, N. Lanata, J. A. Miwa, P. Hofmann, J. Katoch, and S. Ulstrup, "Observation of electrically tunable van Hove singularities in twisted bilayer graphene from nanoARPES," Adv. Mater. **32**, 2001656 (2020).

[21] P. Majchrzak, R. Muzzio, A. J. H. Jones, D. Curcio, K. Volckaert, D. Biswas, J. Gobbo, S. Singh, J. T. Robinson, K. Watanabe, T. Taniguchi, T. K. Kim, C. Cacho, J. A. Miwa, P. Hofmann, J. Katoch, and S. Ulstrup, "In operando angle-resolved photoemission spectroscopy with nanoscale spatial resolution: Spatial mapping of the electronic structure of twisted bilayer graphene," Small Sci. **1**, 2000075 (2021).

[22] N. Dale, M. I. B. Utama, D. Lee, N. Leconte, S. Zhao, K. Lee, T. Taniguchi, K. Watanabe, C. Jozwiak, A. Bostwick, E. Rotenberg, R. J. Koch, J. Jung, F. Wang, and A. Lanzara, "Layer-dependent interaction effects in the electronic structure of twisted bilayer graphene devices," Nano Lett. **23**, 6799–6806 (2023).

[23] S. Riccò, M. Kim, A. Tamai, S. McKeown Walker, F. Y. Bruno, I. Cucchi, E. Cappelli, C. Besnard, T. K. Kim, P. Dudin, M. Hoesch, M. J. Gutmann, A. Georges, R. S. Perry, and F. Baumberger, "In situ strain tuning of the metal-insulator-transition of Ca_2RuO_4 in angle-resolved photoemission experiments," Nat. Commun. **9**, 4535 (2018).

[24] V. Sunko, E. Abarca Morales, I. Marković, M. E. Barber, D. Milosavljević, F. Mazzola, D. A. Sokolov, N. Kikugawa, C. Cacho, P. Dudin, H. Rosner, C. W. Hicks, P. D. C. King, and A. P. Mackenzie, "Direct observation of a uniaxial stress-driven Lifshitz transition in Sr_2RuO_4," npj Quantum Mater. **4**, 46 (2019).

[25] E. Abarca Morales, G.-R. Siemann, A. Zivanovic, P. A. E. Murgatroyd, I. Marković, B. Edwards, C. A. Hooley, D. A. Sokolov, N. Kikugawa, C. Cacho, M. D. Watson, T. K. Kim, C. W. Hicks, A. P. Mackenzie, and P. D. C. King, "Hierarchy of Lifshitz transitions in the surface electronic structure of Sr_2RuO_4 under uniaxial compression," Phys. Rev. Lett. **130**, 096401 (2023).

[26] D. N. Basov, R. D. Averitt, and D. Hsieh, "Towards properties on demand in quantum materials," Nat. Mater. **16**, 1077–1088 (2017).

[27] D. M. Kennes, M. Claassen, L. Xian, A. Georges, A. J. Millis, J. Hone, C. R. Dean, D. N. Basov, A. N. Pasupathy, and A. Rubio, "Moiré heterostructures as a condensed-matter quantum simulator," Nat. Phys. **17**, 155–163 (2021).

[28] M. Cattelan and N. A. Fox, "A perspective on the application of spatially resolved ARPES for 2D materials," Nanomaterials **8**, 284 (2018).

[29] P. Hofmann, "Accessing the spectral function of in operando devices by angle-resolved photoemission spectroscopy," AVS Quantum Sci. **3**, 021101 (2021).

[30] Z. Jiang, K. Hsieh, A. J. H. Jones, P. Majchrzak, C. Sahoo, K. Watanabe, T. Taniguchi, J. A. Miwa, Y. P. Chen, and S. Ulstrup, "Revealing flat bands and hybridization gaps in a twisted bilayer graphene device with microARPES," 2D Mater. **10**, 045027 (2023).

[31] D. Curcio, A. J. H. Jones, R. Muzzio, K. Volckaert, D. Biswas, C. E. Sanders, P. Dudin, C. Cacho, S. Singh, K. Watanabe, T. Taniguchi, J. A. Miwa, J. Katoch, S. Ulstrup, and P. Hofmann, "Accessing the spectral function in a current-carrying device," Phys. Rev. Lett. **125**, 236403 (2020).

[32] D. Curcio, C. E. Sanders, A. Chikina, H. E. Lund, M. Bianchi, V. Granata, M. Cannavacciuolo, G. Cuono, C. Autieri, F. Forte, G. Avallone, A. Romano, M. Cuoco, P. Dudin, J. Avila, C. Polley, T. Balasubramanian, R. Fittipaldi, A. Vecchione, and P. Hofmann, "Current-driven insulator-to-metal transition without Mott breakdown in Ca_2RuO_4," Phys. Rev. B **108**, L161105 (2023).

[33] A. J. H. Jones, R. Muzzio, S. Pakdel, D. Biswas, D. Curcio, N. Lanatà, P. Hofmann, K. M. McCreary, B. T. Jonker, K. Watanabe, T. Taniguchi, S. Singh, R. J. Koch, C. Jozwiak, E. Rotenberg, A. Bostwick, J. A. Miwa, J. Katoch, and S. Ulstrup, "Visualizing band structure hybridization and superlattice effects in twisted MoS_2/WS_2 heterobilayers," 2D Mater. **9**, 015032 (2021).

[34] S. Lisi, X. Lu, T. Benschop, T. A. de Jong, P. Stepanov, J. R. Duran, F. Margot, I. Cucchi, E. Cappelli, A. Hunter, A. Tamai, V. Kandyba, A. Giampietri, A. Barinov, J. Jobst, V. Stalman, M. Leeuwenhoek, K. Watanabe, T. Taniguchi, L. Rademaker, S. J. van der Molen, M. P. Allan, D. K. Efetov, and F. Baumberger, "Observation of flat bands in twisted bilayer graphene," Nat. Phys. **17**, 189–193 (2021).

[35] M. I. B. Utama, R. J. Koch, K. Lee, N. Leconte, H. Li, S. Zhao, L. Jiang, J. Zhu, K. Watanabe, T. Taniguchi, P. D. Ashby, A. Weber-Bargioni, A. Zettl, C. Jozwiak, J. Jung, E. Rotenberg, A. Bostwick, and F. Wang, "Visualization of the flat electronic band in twisted bilayer graphene near the magic angle twist," Nat. Phys. **17**, 184–188 (2021).

[36] Z. Jiang, D. Lee, A. J. H. Jones, Y. Park, K. Hsieh, P. Majchrzak, C. Sahoo, T. S. Nielsen, K. Watanabe, T. Taniguchi, P. Hofmann, J. A. Miwa, Y. P. Chen, J. Jung,

and S. Ulstrup, "Direct view of gate-tunable miniband dispersion in graphene superlattices near the magic twist angle," ACS Nano **19**, 2379–2387 (2025).
[37]A. J. H. Jones, L. Gammelgaard, M. O. Sauer, D. Biswas, R. J. Koch, C. Jozwiak, E. Rotenberg, A. Bostwick, K. Watanabe, T. Taniguchi, C. R. Dean, A.-P. Jauho, P. Bøggild, T. G. Pedersen, B. S. Jessen, and S. Ulstrup, "Nanoscale view of engineered massive Dirac quasiparticles in lithographic superstructures," ACS Nano **16**, 19354–19362 (2022).
[38]H. Iwasawa, P. Dudin, K. Inui, T. Masui, T. K. Kim, C. Cacho, and M. Hoesch, "Buried double CuO chains in $YBa_2Cu_4O_8$ uncovered by nano-ARPES," Phys. Rev. B **99**, 140510 (2019).
[39]S. W. Jung, L. C. Rhodes, M. D. Watson, D. V. Evtushinsky, C. Cacho, S. Aswartham, R. Kappenberger, S. Wurmehl, B. Büchner, and T. K. Kim, "Strong surface termination dependence of the electronic structure of polar superconductor LaFeAsO revealed by nano-ARPES," New J. Phys. **24**, 113018 (2022).
[40]A. Chikina, G. Bhattacharyya, D. Curcio, C. E. Sanders, M. Bianchi, N. Lanatà, M. Watson, C. Cacho, M. Bremholm, and P. Hofmann, "One-dimensional electronic states in a natural misfit structure," Phys. Rev. Materials **6**, L092001 (2022).
[41]K. Volckaert, P. Majchrzak, D. Biswas, A. J. H. Jones, M. Bianchi, Z. Jiang, R. Dubourg, R. Ø. Stenshøj, M. L. Jensen, N. C. Jones, S. V. Hoffmann, J.-L. Mi, M. Bremholm, X.-C. Pan, Y. P. Chen, P. Hofmann, J. A. Miwa, and S. Ulstrup, "Surface electronic structure engineering of manganese bismuth tellurides guided by micro-focused angle-resolved photoemission," Adv. Mater. **35**, 2301907 (2023).
[42]M. D. Watson, P. Dudin, L. C. Rhodes, D. V. Evtushinsky, H. Iwasawa, S. Aswartham, S. Wurmehl, B. Büchner, M. Hoesch, and T. K. Kim, "Probing the reconstructed fermi surface of antiferromagnetic $BaFe_2As_2$ in one domain," npj Quantum Mater. **4**, 36 (2019).
[43]L. C. Rhodes, M. D. Watson, A. A. Haghighirad, D. V. Evtushinsky, and T. K. Kim, "Revealing the single electron pocket of FeSe in a single orthorhombic domain," Phys. Rev. B **101**, 235128 (2020).
[44]P. Dudin, P. Lacovig, C. Fava, E. Nicolini, A. Bianco, G. Cautero, and A. Barinov, "Angle-resolved photoemission spectroscopy and imaging with a submicrometre probe at the SPECTROMICROSCOPY-3.2 L beamline of Elettra," J. Synchrotron Radiat. **17**, 445–450 (2010).
[45]A. Bostwick, E. Rotenberg, J. Avila, and M. C. Asensio, "Zooming in on electronic structure: NanoARPES at SOLEIL and ALS," Synchrotron Radiat. News **25**, 19–25 (2012).
[46]J. Avila and M. C. Asensio, "First nanoARPES user facility available at SOLEIL: An innovative and powerful tool for studying advanced materials," Synchrotron Radiat. News **27**, 24–30 (2014).
[47]R. J. Koch, C. Jozwiak, A. Bostwick, B. Stripe, M. Cordier, Z. Hussain, W. Yun, and E. Rotenberg, "Nano focusing of soft x-rays by a new capillary mirror optic," Synchrotron Radiat. News **31**, 50–52 (2018).
[48]B. Rösner, P. Dudin, J. Bosgra, M. Hoesch, and C. David, "Zone plates for angle-resolved photoelectron spectroscopy providing sub-micrometre resolution in the extreme ultraviolet regime," J. Synchrotron Radiat. **26**, 467–472 (2019).
[49]H. Gao, H. Xiao, F. Wang, F. Zhu, M. Wang, Z. Liu, Y. Chen, and C. Chen, "Nano-ARPES endstation at BL07U of shanghai synchrotron radiation facility," Synchrotron Radiat. News **37**, 12–17 (2024).
[50]C. Kastl, R. J. Koch, C. T. Chen, J. Eichhorn, S. Ulstrup, A. Bostwick, C. Jozwiak, T. R. Kuykendall, N. J. Borys, F. M. Toma, S. Aloni, A. Weber-Bargioni, E. Rotenberg, and A. M. Schwartzberg, "Effects of defects on band structure and excitons in WS_2 revealed by nanoscale photoemission spectroscopy," ACS Nano **13**, 1284–1291 (2019).
[51]J. Katoch, S. Ulstrup, R. J. Koch, S. Moser, K. M. McCreary, S. Singh, J. Xu, B. T. Jonker, R. K. Kawakami, A. Bostwick, E. Rotenberg, and C. Jozwiak, "Giant spin-splitting and gap renormalization driven by trions in single-layer WS_2/h-BN heterostructures," Nat. Phys. **14**, 355–359 (2018).
[52]S. Ulstrup, R. J. Koch, S. Singh, K. M. McCreary, B. T. Jonker, J. T. Robinson, C. Jozwiak, E. Rotenberg, A. Bostwick, J. Katoch, and J. A. Miwa, "Direct observation of minibands in a twisted graphene/WS_2 bilayer," Sci. Adv. **6**, eaay6104 (2020).
[53]S. . Ý. Ágústsson, A. J. H. Jones, D. Curcio, S. Ulstrup, J. Miwa, D. Mottin, P. Karras, and P. Hofmann, "Autonomous micro-focus angle-resolved photoemission spectroscopy," Rev. Sci. Instrum. **95**, 055106 (2024).
[54]N. Hertel and S. V. Hoffmann, "ASTRID2: A new Danish low-emittance SR source," Synchrotron Radiat. News **24**, 19–23 (2011).
[55]H. Kjeldsen, F. Folkmann, J. . v. Elp, H. Knudsen, J. B. West, and T. Andersen, "Absolute measurements of photoionization cross-sections for ions," Nucl. Instrum. Methods Phys. Res., Sect. B **234**, 349–361 (2005).
[56]B. Jensen, S. Butorin, T. Kaurila, R. Nyholm, and L. Johansson, "Design and performance of a spherical grating monochromator used at MAX I," Nucl. Instrum. Methods Phys. Res., Sect. A **394**, 243–250 (1997).
[57]C. Chen, "Concept and design procedure for cylindrical element monochromators for synchrotron radiation," Nucl. Instrum. Methods Phys. Res., Sect. A **256**, 595–604 (1987).
[58]K. Radler and J. Berkowitz, "Photoionization mass spectrometry of neon using synchrotron radiation: Anomalous variation of resonance widths in the noble gases," J. Chem. Phys. **70**, 216–220 (1979).
[59]N. Dale, R. Mori, M. I. B. Utama, J. D. Denlinger, C. Stansbury, C. G. Fatuzzo, S. Zhao, K. Lee, T. Taniguchi, K. Watanabe, C. Jozwiak, A. Bostwick, E. Rotenberg, R. J. Koch, F. Wang, and A. Lanzara, "Correlation-driven electron-hole asymmetry in graphene field effect devices," npj Quantum Mater. **7**, 9 (2022).
[60]M. M. Otrokov, I. I. Klimovskikh, H. Bentmann, D. Estyunin, A. Zeugner, Z. S. Aliev, S. Gaß, A. U. B. Wolter, A. V. Koroleva, A. M. Shikin, M. Blanco-Rey, M. Hoffmann, I. P. Rusinov, A. Y. Vyazovskaya, S. V. Eremeev, Y. M. Koroteev, V. M. Kuznetsov, F. Freyse, J. Sánchez-Barriga, I. R. Amiraslanov, M. B. Babanly, N. T. Mamedov, N. A. Abdullayev, V. N. Zverev, A. Alfonsov, V. Kataev, B. Büchner, E. F. Schwier, S. Kumar, A. Kimura, L. Petaccia, G. Di Santo, R. C. Vidal, S. Schatz, K. Kißner, M. Ünzelmann, C. H. Min, S. Moser, T. R. F. Peixoto, F. Reinert, A. Ernst, P. M. Echenique, A. Isaeva, and E. V. Chulkov, "Prediction and observation of an antiferromagnetic topological insulator," Nature **576**, 416–422 (2019).
[61]X. Wu, J. Li, X.-M. Ma, Y. Zhang, Y. Liu, C.-S. Zhou, J. Shao, Q. Wang, Y.-J. Hao, Y. Feng, E. F. Schwier, S. Kumar, H. Sun, P. Liu, K. Shimada, K. Miyamoto, T. Okuda, K. Wang, M. Xie, C. Chen, Q. Liu, C. Liu, and Y. Zhao, "Distinct topological surface states on the two terminations of $MnBi_4Te_7$," Phys. Rev. X **10**, 031013 (2020).
[62]J. Wu, F. Liu, C. Liu, Y. Wang, C. Li, Y. Lu, S. Matsuishi, and H. Hosono, "Toward 2D magnets in the $(MnBi_2Te_4)(Bi_2Te_3)_n$ bulk crystal," Adv. Mater. **32**, 2001815 (2020).
[63]C. Liu, Y. Wang, H. Li, Y. Wu, Y. Li, J. Li, K. He, Y. Xu, J. Zhang, and Y. Wang, "Robust axion insulator and chern insulator phases in a two-dimensional antiferromagnetic topological insulator," Nat. Mater. **19**, 522–527 (2020).
[64]Y. Deng, Y. Yu, M. Z. Shi, Z. Guo, Z. Xu, J. Wang, X. H. Chen, and Y. Zhang, "Quantum anomalous hall effect in intrinsic magnetic topological insulator $MnBi_2Te_4$," Science **367**, 895–900 (2020).
[65]R. C. Vidal, A. Zeugner, J. I. Facio, R. Ray, M. H. Haghighi, A. U. B. Wolter, L. T. Corredor Bohorquez, F. Caglieris, S. Moser, T. Figgemeier, T. R. F. Peixoto, H. B. Vasili, M. Valvidares, S. Jung, C. Cacho, A. Alfonsov, K. Mehlawat, V. Kataev, C. Hess, M. Richter, B. Büchner, J. van den Brink, M. Ruck, F. Reinert, H. Bentmann, and A. Isaeva, "Topological electronic structure and intrinsic magnetization in $MnBi_4Te_7$: A Bi_2Te_3 derivative with a periodic Mn sublattice," Phys. Rev. X **9**, 041065 (2019).
[66]S. Tian, S. Gao, S. Nie, Y. Qian, C. Gong, Y. Fu, H. Li, W. Fan, P. Zhang, T. Kondo, S. Shin, J. Adell, H. Fedderwitz, H. Ding, Z. Wang, T. Qian, and H. Lei, "Magnetic topological insulator $MnBi_6Te_{10}$ with a zero-field ferromagnetic state and gapped Dirac surface states," Phys. Rev. B **102**, 035144 (2020).
[67]X.-M. Ma, Z. Chen, E. F. Schwier, Y. Zhang, Y.-J. Hao, S. Kumar, R. Lu, J. Shao, Y. Jin, M. Zeng, X.-R. Liu, Z. Hao, K. Zhang, W. Mansuer, C. Song, Y. Wang, B. Zhao, C. Liu, K. Deng, J. Mei, K. Shimada, Y. Zhao, X. Zhou, B. Shen, W. Huang, C. Liu, H. Xu, and C. Chen, "Hybridization-induced gapped and gapless

states on the surface of magnetic topological insulators," Phys. Rev. B **102**, 245136 (2020).
[68]R. C. Vidal, H. Bentmann, J. I. Facio, T. Heider, P. Kagerer, C. I. Fornari, T. R. F. Peixoto, T. Figgemeier, S. Jung, C. Cacho, B. Büchner, J. van den Brink, C. M. Schneider, L. Plucinski, E. F. Schwier, K. Shimada, M. Richter, A. Isaeva, and F. Reinert, "Orbital complexity in intrinsic magnetic topological insulators $MnBi_4Te_7$ and $MnBi_6Te_{10}$," Phys. Rev. Lett. **126**, 176403 (2021).
[69]S. V. Borisenko, T. K. Kim, A. A. Kordyuk, M. Knupfer, J. Fink, J. E. Gayone, P. Hofmann, H. Berger, B. Liang, A. Maljuk, and C. T. Lin, "Excitation energy dependence of the ARPES intensity in Pb-doped and pristine $Bi_2Sr_2CaCu_2O_{8+\delta}$," Physica C **417**, 1–6 (2004).
[70]C. Yan, S. Fernandez-Mulligan, R. Mei, S. H. Lee, N. Protic, R. Fukumori, B. Yan, C. Liu, Z. Mao, and S. Yang, "Origins of electronic bands in the antiferromagnetic topological insulator $MnBi_2Te_4$," Phys. Rev. B **104**, L041102 (2021).